Low-strain fatigue in 316L steel surface grains, a three dimension discrete dislocation dynamics modelling of the early cycles. Part-2: Persistent slip markings and micro-crack nucleation

Christophe Depres, Christian Robertson, Marc C. Fivel

Low-strain fatigue in 316L steel surface grains, a three dimension discrete dislocation dynamics modelling of the early cycles.
Part-2: Persistent slip markings and micro-crack nucleation

Journal:	*Philosophical Magazine & Philosophical Magazine Letters*
Manuscript ID:	TPHM-05-Jun-0306.R1
Journal Selection:	Philosophical Magazine
Date Submitted by the Author:	25-Aug-2005
Complete List of Authors:	depres, christophe; LMECA, Universite de Savoie robertson, christian; CEA/Saclay, DMN Fivel, Marc; GPM2, CNRS / INPG
Keywords:	fatigue, dislocations
Keywords (user supplied):	crack initiation

Low-strain fatigue in 316L steel surface grains, a three dimension discrete dislocation dynamics modelling of the early cycles. Part-2: Persistent slip markings and micro-crack nucleation

C. Déprés[†‡], C.F. Robertson[*†], M.C. Fivel[‡]
[†] CEA/Saclay, SRMA, 91191 Gif-sur-Yvette, France
[‡] GPM2, CNRS/INPG, BP 46, 101 Rue de la Physique, 38 402 St Martin d'Hères, France

ABSTRACT

The early stages of formation of persistent slip markings in fatigue are analysed, using three-dimensional discrete dislocation dynamics modelling. The surface displacements due to slip are computed using a specific post-processing method. Fatigue simulations under various strain ranges and grain sizes have been performed. The resulting surface slip markings and their evolutions are analyzed quantitatively, in terms of the marking height and thickness. A detailed scheme for persistent slip marking formation and morphology is proposed, in relation to the persistent slip-band dislocation arrangements present within the grain. The simulations show the crucial role of these arrangements for the extrusion-intrusion growth and localisation of slip at the band edges. Local stress concentrations inside the crystal and their relations to damage initiation are also analysed. The results provide insights for an original micro-crack initiation scheme, combining different initiation mechanisms as described in the literature.

[*] To whom all correspondence should be addressed.

1. INTRODUCTION

One characteristic feature of fatigue testing in ductile metals is strain localization in the form of persistent slip markings (PSMs), at the specimen surface [1]. Thanks to numerous experimental studies, it is now well established that the presence of the PSM is the origin of fatigue crack initiation [2-4]. During the fatigue tests, high resolution examination of either the specimen surface [1, 5-8] or the dislocation microstructure [9-13] is possible, though not in the same grain or crystal, due to the destructive character of thin foil preparation for transmission electron microscopy. For this and other reasons, a description of the details of surface relief formation and their relations with the dislocation microstructures inside the grains are difficult to establish. Knowledge of these details is nevertheless crucial for the understanding of crack initiation mechanisms and, ultimately, to propose better fatigue life prediction models. One existing method for studying the details of intra-granular dislocation activity is three dimensional discrete dislocation dynamics (DDD) modelling [14-18].

This type of modelling was proved valuable for analysing dislocation-based local plasticity problems, such as plastic instabilities [19-20], fatigue [21], nano-indentation [22] or thin film growth and deformation [23-24]. Here, the surface displacements due to dislocation slip and elimination at the surface are computed using a newly developed post-processing method [25-26]. This way, the surface displacements associated with the DDD simulated dislocation microstructures can be imaged in details. The simulation results are compared with experimental results for partial validation.

2. FATIGUE SIMULATIONS IN SURFACE GRAINS

2.1 Model overview

The DDD formalism, load control methods and material parameters (for 316L steel) used here are exactly the same as described in accompanying part I paper [27]. The applied loading is monitored for imposed plastic strain conditions, satisfying the quasi-static assumption. All simulations are performed in isothermal conditions, at 300K. The simulated grain diameters are within a range of 10 to 22 μm, whereas the applied plastic strain range is $\Delta\varepsilon_p = 10^{-3}$ (in single slip) unless otherwise specified. In simulated surface grains, dislocations are free to escape on one top surface, whereas all other surfaces act as strong obstacles to dislocation motion, as would be the case for highly disordered grain boundaries. Each dislocation segment leaving the crystal through the top boundary creates a step in the surface, with a step height of one b, the magnitude of the Burgers vector. This effect of plasticity on surface topography is computed here using a special post-treatment method as described in the next section. Most of the simulations are performed in symmetrical applied plastic strain conditions ($\varepsilon_{p,min} = -\varepsilon_{p,max}$). Simulations under non-symmetrical conditions have also been performed ($\varepsilon_{p,min} \neq -\varepsilon_{p,max}$), for comparison purposes. Surface profiles obtained in double slip are examined as well, with a view to study the effect of multi-axial loading conditions on surface plasticity.

In theory, the surface of a defect free solid crystal satisfies the traction free boundary condition (see for example [25, 28-29]). This condition generates stresses within a sub-surface layer of material: the so-called image-forces. Here, the image-forces are neglected and a homogeneous applied load within the simulated grain has been selected. This choice of simple

boundary conditions is made for the purpose of facilitating the interpretation of the results. Simulation results obtained with other boundary conditions are described in Appendix-1, in support of the results and analysis presented in section-3 of this paper.

The inert environment is reported to have little influence on the kinetics of surface relief formation though it significantly affects crack initiation and propagation [30-33]. In this study, environmental effects are not accounted for.

2.2 Surface displacement computation method

In the DDD modelling framework, the dislocations are treated as elastic inclusions embedded in an infinite elastic medium, via the analytical expressions used to compute their associated long-range stress fields. In the same fashion, the analytical elastic displacement solutions for finite dislocation segments can be used to compute the dislocation displacements anywhere in the simulated volume, including in the grain surface. In simulation boxes representative of bulk grains, i.e. where all the surfaces are impassable, the dislocation microstructure is made up of closed dislocation loops only. In this case, the use of Barnett's solution adapted to the displacement field due to triangular dislocation loops is straightforward (see [34] and figure 1a). In figure 1b, the displacement field for an arbitrarily shaped dislocation loop is derived by superimposing the displacement contributions of as many single triangular loops as needed, so as to cover the entire loop. The triangles are constructed using one closing point O per slip plane. The general case of non-planar dislocation loops e.g. with cross-slipped parts, has been described in [27].

[Insert figure 1 about here]

Unlike for bulk grains, some of the dislocation loops present in surface grains are cut and left open, a process responsible for surface step formation (see figure 2a). In surface grains therefore, Barnett's expression can no longer be used without a special, ad-hoc treatment. One simple way to deal with the open loop problem consists in adding new virtual dislocation segments outside of the simulated crystal, as first proposed by Weygand *et al.* [25] (see figure 2b). This method is systematically implemented in surface grain simulations, by using simulation boxes divided into two distinct parts. The lower part is the crystalline volume, while the upper part is a virtual medium, containing the virtual segments.

In this configuration, the grain surface is the separation plane between the lower and upper parts of the simulation box. The virtual surface is a two-dimensional array of calculation points *M*, positioned exactly on the crystal/virtual-medium boundary. The surface displacement at each calculation point is determined at fixed time intervals, using the same method as described in figure 1. The spatial resolution of the surface profiles depends on the discrete spacing of calculation points.

Particular rules have to be defined in order to make sure that the motion of the dislocations left in the crystal is not arbitrarily modified by the presence of the virtual segments. Hence, cross-slip and Frank-Read multiplication mechanisms are shut down in the virtual medium, and so are the interaction stresses coming from the virtual dislocations.

[Insert figure 2 about here]

The choice of the virtual volume size is made in consideration of the following arguments. The plot in figure 3b shows the surface displacements of a dislocation shear loop obtained when the virtual (edge) segments are placed at distance h, above the virtual surface. The calculations yield the correct surface displacement (a one b high step), provided h is larger than 1 µm. In practice, virtual medium of at least 5 µm in thickness is used, to ensure that all the virtual segments generated during all the simulated cycles are stored at least 1 µm away from the virtual surface. The virtual dislocations are stored in the same order as they leave the crystal, in order to keep the bookkeeping of the surface relief evolution as simple as possible.

[Insert figure 3 about here]

In the present DDD model, virtual dislocation coming back into the crystal medium is equivalent to dislocation nucleation from the surface. In theory, such phenomenon is possible, especially when sharp surface profiles are present [35]. Dislocation emission from the surface is neglected here by keeping the virtual dislocations within the virtual medium, i.e. by preventing any return into the crystal medium. This way, a step printed on the surface can only be erased provided a loop of opposite sign emitted from within the volume reaches the surface on exactly the same slip plane.

3 RESULTS

3.1 Slip induced surface displacements

3.1.1 Surface markings and associated dislocation microstructures

Fatigue simulations ($\Delta\varepsilon_p \leq 10^{-3}$) performed in symmetrical conditions exhibit two distinct regimes, namely the initial and saturation regimes (see part I accompanying paper [27] for details). In the initial regime, the dislocation density grows rapidly, while the stress amplitude is the highest. Then, as the cycles proceed, the average dislocation densities saturate, while dislocation density fluctuations of stable magnitude are observed from one cycle to the other. As the number of cycles N gets closer to the saturation regime, i.e. $N = N_{sat}$, the stress amplitude gradually relaxes towards a lower, stabilized value (in the simulations N_{sat} = 2 to 10 cycles). During the initial regime, most of the surface steps are reversible: a reversible step made during forward loading, either positive or negative, is erased when the load sign is reversed, until a step of opposite sign is formed. The reversible steps formed during the initial regime are distributed uniformly in the grain surface (see figure 4, cycle 3). These steps are associated with the early formed pile-ups.

In a few locations, irreversible markings start forming at the onset of the saturation regime ($N = N_s$). The saturation stage corresponds to the formation of the persistent slip-band dislocation arrangements within the grain. The main features of the numerically generated persistent slip bands are described in Part I accompanying paper. These features include: immobile inter-channel tangles, high mobility pile-ups at the PSB-matrix interfaces and potentially mobile multi-polar walls inside the channels (see figure 5). It is worth recalling that the channel notion used in this paper is original and different from the usual channel description. It refers to tube or chimney-like arrangements of regularly spaced multi-poles (see figure 5b and 5c) made of prismatic loops with the same area as the channel cross-section, i.e. the section perpendicular to the Burgers vector. The channel length corresponds to the grain depth in the direction of the Burgers vector. Unlike the reversible slip markings, the

irreversible surface markings are not erased upon load suppression or reversal. This process results in gradual extrusion growth. Irreversible intrusions are also formed, though in smaller quantities. When extrusion (intrusion) growth proceed ($N > N_{sat}$), reversible surface slip activity stops everywhere except on the two edges of the persistent extrusions (intrusion), as shown in figure 4 cycle n°23. This numerical result is consistent with experimental results in single or poly-crystals: the largest slip offsets are found at the PSB-matrix interfaces (Ma and Laird 1989). The reversible surface markings present after saturation are associated with the PSB-matrix interfacial pile-ups as described in part I.

[Insert figure 4 about here]

The thicknesses of the persistent surface slip markings are the same as the persistent slip band thickness measured inside the grain. The thickness data obtained in the simulated surface is quite consistent with both AFM surface data and TEM observations (200-500 nm), for specimens cycled at the same plastic strain range. The persistent slip band arrangements are characterized by a thickness e_i, a mean spacing d_i and a number of bands per grain n. The variability of these quantities in the various simulations has been treated in part I accompanying paper [27].

[Insert figure 5 about here]

The irreversible surface displacements displayed in figs. 4, 5 and 6 are rather tongue-like than ribbon-like. The individual tongues are made of parallelograms of the same area as the typical channel cross-section (see figure 6). Loop motions inside the channels are sporadic jumps parallel to the primary Burgers vector, over distances corresponding to one multi-pole

interspacing (about 500 nm, see figure 5c). These motions or jumps concern either individual loops or multi-poles as a whole. In all cases, the channel loop motions are triggered by short-distance interactions with the highly mobile dislocations inside the interfacial pile-ups. Nevertheless, the extrusion growth is a relatively slow process as compared with the reversible slip activity, the latter being synchronous with the applied load changes.

When the applied plastic strain range is slightly increased, the channel cross sections become elongated, in the direction parallel to the slip bands or markings (in direction parallel to $\bar{1}3\bar{4}$, see figure 5). For example, in simulations performed with $\Delta\varepsilon_p = 1.6\times10^{-3}$ (not shown here), the typical channel width is doubled as compared to that in figure 5b. Then, the surface displacements associated with such channels become more ribbon-like than tongue-like, as seen for example in [1, 6].

[Insert figure 6 about here]

3.1.2 Surface marking growth rate

In general, it is difficult to evaluate the mean extrusion heights *h* directly from surface profiles as in figure 5 or figure 6, due to the three-dimensional character of the markings. For this reason and for the purpose of systematic comparisons with experimental data, an automatic, simplified surface slip-marking characterization method is preferred. Figure 7 displays a typical dislocation loop in a surface grain simulation, including the virtual dislocation used to compute the surface displacements. The surface displacements associated with the individual loops is given by the quantity *a* (see figure 7), defined as the length of the edge part of the virtual segments projected on the unit vector **n**, perpendicular to the crystal surface. The total

surface displacement at a given time-step is obtained by adding up the quantities *a* from all the dislocation segments present in the virtual medium: $a_{tot} = \Sigma_{virtual} |a|$.

[Insert figure 7 about here]

From quantity a_{tot}, an approximation of the average extrusion height *h* can be derived, by assuming that the dominant contribution to a_{tot} comes indeed from the persistent slip markings. As depicted in figure 4, this is a very good approximation, provided $N > N_s$. By further assuming a simple dented profile for the markings (arbitrary width), the single extrusion height at a particular time step is then given by the simple expression:

$$h \approx a_{tot} (b / 2ND) \quad (1)$$

where a_{tot} is the surface displacements coming from all the dislocation microstructures, b is the Burgers vector magnitude, *N* the number of slip bands inside the grain and D the grain diameter. In figure 8a, the dimensionless quantity a_{tot}/D is plotted in single- and double-slip, under symmetrical loading conditions and for the same equivalent plastic strain range. In both cases, the surface marking growth rate is random walk-like, i.e. proportional to $N^{1/2}$, though with a different pre-factor, i.e. α in single slip, 4α in double slip.

By extrapolating the results in figure 8a up to cycles N = 1200 and by using expression (1), an average extrusion growth rate of 0.05 nm per cycle is obtained, between cycle N = 1000 and N = 1200. This value is consistent with the AFM data reported in Man 2003 for $\Delta\varepsilon_p = 2\times10^{-3}$, as far as the early extrusion growth regime is considered (N < 2000 cycles). This indicates that slip is an important contribution to the early extrusion rate.

Later in the cycles, a large difference exists between the simulation results and the experimental data, yielding a linear growth regime for the latter instead of a random walk-like regime for the former. Thus, other mechanisms have to be considered to account for the experimental topographic data, such as point defect production and migration, as stressed in [1].

[Insert figure 8 about here]

As mentioned earlier, for a given grain diameter, the a_{tot}/D accumulation rate computed in double slip is four times as fast as in single-slip conditions. In double slip however, the number of individual PSB inside the grain is four times as large as in single slip. This increase in the number of slip bands probably comes from the number of cross-slip events per time-unit in double slip, which is exactly four time as high as in single slip. Hence, the growth rates and the heights of the individual slip markings obtained using expression (1) are exactly the same, in both cases. This result is consistent with the experimental results reported in Man 2002: surface relief is the same for grains oriented for double or single slip, since the individual slip bands carry the same amount of slip.

The simulations also provide information regarding the effect of strain range and grain size. For a fixed grain size D and a given cycle N, the quantity a_{tot}/D is found to be a linear function of the strain range $\Delta\varepsilon_p$. For fixed plastic strain range $\Delta\varepsilon_p$ and cycle N, the quantity a_{tot}/D is a linear function of the grain size D.

Simulations in non-symmetric loading conditions ($\varepsilon_{p,max} \neq -\varepsilon_{p,min}$) have been performed for comparison purposes. The results are shown in figure 8b, for the same total plastic strain

range $\Delta\varepsilon_p = 1\times10^{-3}$. The imposed mean strain has a strong effect on the surface displacement accumulation rate, since the evolution of quantity a_{tot}/D is no longer proportional to $N^{1/2}$. The exponent magnitude applied to quantity N instead depends on the magnitude of the mean strain $\varepsilon_p^{moy} \neq 0$, though not in a straightforward, linear fashion. More work would be required to establish the exact form of this dependence. Hence, the main conclusion to be drawn from the $\varepsilon_p^{moy} \neq 0$ simulations is an acceleration of the persistent surface marking growth rate. In all these calculations, the mean stress relaxation was slow, due to the relatively small loading amplitude. Therefore, similar conclusions concerning the surface offset could have been obtained with $\sigma^{moy} \neq 0$ simulations instead of $\varepsilon_p^{moy} \neq 0$ simulations.

It is worth recalling that the presented results have been obtained without taking into account the image forces induced by the free surface. In real surface grains, image forces are present in the sub-surface region, as mentioned in section 2.1. In theory, a defect-free surface generates an attractive image force-field. In 316L stainless steel however, the surfaces are not defect-free. This material is indeed corrosion-resistant thanks to a hard (and brittle) passive oxide layer, with an elastic modulus that is much larger than that of the underlying metallic substrate. In that case, dislocations approaching the surface undergo repulsive, instead of attractive image forces. Therefore, the determination of realistic boundary conditions is not straightforward and needs a separate and thorough investigation. Nevertheless, the simple case of an ideal free surface is treated in Appendix-1. Qualitatively, the results support the analysis presented in sections 3.1 and 3.2: no significant changes were observed when using free surface boundary conditions, neither in the persistent slip band characteristics nor in the slip marking geometries. In fatigue therefore, the results relate more strongly with the deformation mechanisms inside the grain than to the direct surface/dislocation interactions.

3.2 Micro-crack initiation analysis using DDD results

The existing micro-crack formation models in fatigue can be sorted into two main categories (see [4, 36] for a review): random irreversible slip and localized plane separation.

3.2.1 Random irreversible slip and damage initiation

In this first model category, micro-crack initiation results from random irreversible slip mechanisms, as proposed earlier by [37-40]. In these models, micro-crack initiation is directly related to the continuous intrusion growth. In the DDD simulations performed here in symmetrical loading conditions, extrusion (intrusion) growth results from channel dislocation loop elimination on the surface. Hence, once the PSB have formed, slip is no longer randomly distributed among all the parallel slip planes inside the crystal. Thus, coarse random slip present here relates to the PSB-matrix edges only, where interfacial pile-ups are present. Hence, the parallel active plane separation is given by the individual PSB width, as in a more recent two dimensional coarse slip model adapted to single crystals [41]. In this model, both the slip offset and the associated irreversibility fraction are pre-imposed. The micro-crack initiation in a single crystal is defined as a 3 µm deep intrusion, which is obtained after reaching 3459 cycles, for $\Delta\varepsilon_p = 4\times10^{-3}$. In the present DDD modelling, the slip offset and irreversibility in the active slip planes are not imposed in any way. Such quantities emerge as a natural outcome and also account for grain boundary effects. In spite of these differences, a coarse-slip type of extrusion growth is obtained, according to a $N^{1/2}$ function. In the future rigorous, direct comparisons between two dimensional coarse slip models and DDD results could be established, for example by using boundary conditions representative of single crystals and performing a much larger number of simulated cycles.

3.2.2 Localized plane separation and damage initiation

In this second damage-initiation model category, a clear distinction is made between intrusions and micro-cracks. Hence, initiation is either due to the loss of coherence across a slip plane induced by an accumulation of dislocations in two nearby, parallel slip planes [42], or local cleavage-like slip plane separation. Quite generally, local accumulation of dislocations can promote both loss of coherence and cleavage-like mechanisms, through the long range stress fields associated with the local, high dislocation density arrangements. The DDD modelling results are one of the best-suited methods for studying such distortion stress (or energy) concentrations, within realistic PSB structures. At a given time-step, the total elastic energy stored in the crystal is the sum of two terms, namely the macroscopic elastic energy, due to the homogeneous crystal lattice distortion contribution:

$$\frac{1}{2}\int_V K^{-1}_{ijkl}\sigma^{applied}_{ij}\sigma^{applied}_{kl}\mathbf{dV} \quad (2)$$

plus the microscopic elastic energy, due to the heterogeneous dislocation distortion contribution:

$$\frac{1}{2}\int_V K^{-1}_{ijkl}\sigma^{dislocation}_{ij}\sigma^{dislocation}_{kl}\mathbf{dV} \quad (3)$$

The quantity **K** is the fourth-rank stiffness operator. The spatial distribution of the macroscopic energy is assumed to be homogeneous within the crystal, whereas the dislocation distortion is clearly heterogeneous, depending on the local dislocation distribution. This

microscopic term can be the dominant energy contribution in portions of the crystal where a high dislocation density is present. More specifically, it is believed that local distortions can facilitate the permanent local separation of two slip planes, wherever there is:

(i)- a high distortion energy stored in the crystal, acting as a slip plane separation promoter,

(ii)- a sufficient stress tri-axiality, i.e. a stress component normal to the crystal planes to separate, acting as the separation driving force.

Since no damaged zones (micro-cracks) are present inside of the simulation volume, the local stresses coming from the present DDD computations are regarded as sub-threshold values. In the DDD fatigue simulations, N_s is relatively small (2 to 10 cycles) as compared to the total number of simulated cycles N_{tot} (20 to 30 cycles). It is therefore hoped that stress concentration mechanisms operating during cycles $N > N_s$ up to cycle N_{tot} keep on operating afterwards, possibly until damage thresholds are attained. In practice, quantity-(i) is taken as the dislocation distortion energy term only, i.e. it is computed using expression (3). The lattice distortion contribution, -expression (2)-, is associated with the external applied loading and undergoes no long-term evolution after saturation, neither globally nor locally. In single slip conditions, quantity-(ii) is taken as the stress normal to the primary slip plane, which is the usual micro-crack habit plane in surface grains [43].

A- Analysis of the dislocation distortion energies

The energy densities are first computed at fixed time intervals, by evaluating expression (3) in a pre-defined calculation set of points forming a a^3 large cubic array, referred to as a test volume. Test volumes of various sizes can be positioned anywhere within the simulated crystal, for local analysis purposes. Analysis is performed as follows. At time t, the results obtained in all the single calculation points are sorted out into an energy distribution histogram. A typical histogram is plotted in figure 9a. From each Gaussian profile, both the average energy and the standard-deviation of the energy distributions are derived. The histogram tail values come from the calculation points positioned at a very close distance from the dislocation segments. These high values result from the diverging elastic expressions used in the DDD formalism. Thus, they are regarded as non-relevant as far as damage initiation is concerned. Unlike the distribution tails, the energy distribution widths undergo a systematic change, whenever the dislocation relative positions are modified. Hence, a steady growth of the standard-deviation parameter reveals a local energy accumulation activity, due to short-range dislocation re-arrangement mechanisms. Thus, the maximum local energy levels relevant to initiation promotion are proportional to the standard deviation energy parameter.

[Insert figure 9 about here]

All the results displayed in figure 9 are associated with a cubic test volume (with a = 0.5 µm), positioned in the sub-surface region, inside a channel dislocation structure similar to that of figure 5b (see section 3.1.1 for details concerning the channel structures). Inside this test volume, the standard deviation energy parameter increases steadily (see figure 9c), whereas the average energy density saturates quickly (see figure 9b). Analysis of similar test volumes positioned inside the other channels found in the same simulated crystal yield the same

results. On the other hand, no standard-deviation energy changes are obtained in test volumes positioned outside the channels. It is therefore concluded that the local energy accumulation is due to the specific channel dislocation structures. Dislocation distortion energy mappings confirm this point: local energy accumulation takes place within the channels only, where potentially mobile multi-polar dislocation walls are present. It is observed that the high energy zones are about 20-100 nm large, a size consistent with the multi-pole thickness parallel to the Burgers vector (see figure 5c).

B- Analysis of the dislocation distortion stress tensors

In this section, the same data as presented in section *A* is analysed in terms of the dislocation stress tensor components. It appears that the resolved shear stress on the primary system is the only contributing term to the steady increase in energy in the channels (compare figure 10a and 9b). All the other stress components, though significant in magnitude, exhibit no clear evolution during the cycles (see figure 10b). This means that the dislocation microstructures alone do not accumulate further normal stress across the primary slip plane, i.e. the PSB plane.

[Insert figure 10 about here]

One possible alternate origin for local accumulation of normal stress is the geometric singularities associated with the surface slip markings, of either the intrusion or extrusion type. Hence, using analytical or finite element calculations on dented extrusion profiles, it can be shown that normal stress in the near surface region is strongly related to the magnitude of the *h/e* ratio, where *h* is the extrusion height and *e* the extrusion width. Examples of individual

extrusion height growth kinetics in the DDD simulations are plotted in figure 11a, for two grain geometries. The corresponding individual extrusion width evolution is presented in figure 11b. Since the extrusion width *e* is nearly constant after a fast initial expansion stage, the model predicts a similar evolution for the ratio *h/e* as that of the extrusion height *h*. Therefore, tri-axiality in surface grains is present near the surface markings and builds up at the same rate as the extrusion grows.

[Insert figure 11 about here]

C- Micro-crack initiation model

In principle, once the stress concentration evolutions and the damage initiation thresholds are known, time to intrinsic (in absence of point defects and environmental effects) damage initiation can be predicted. The threshold determination is, however, a major issue by itself, which would warrant a separate and detailed study, including atomic scale simulations. Indeed, these threshold quantities are related to the atomic-bound strength and cannot be derived from the elasticity theory. Although damage initiation predictions will not be made here, information from the previous sections *A* and *B* are used to propose a new micro-crack initiation scheme. Quite generally, micro-crack initiation is easier when high-distortion energy is achieved within a crystal portion where significant tri-axiality is present. Here, these most favourable conditions are satisfied each time a large multi-pole (see figure 5c) escapes out of the crystal surface. Then, a significant overstress peak in the subsurface region is generated, as in figure 10a cycle 23. Examination of the dislocation microstructures at the time of that peak reveals that a large multi-pole is present within the analysis volume. Since

the multi-pole is no longer present a few time steps later, its velocity is thus consistent with the short stress peak duration (see also section 3.1.1 for a description of the dislocation motion within the channels).

The proposed micro-crack initiation scheme is compatible with the experimental evidence for crack initiation in ductile metal that shows it is a slow and continuous process, as per the following arguments:

(i)- only one single high-dislocation density wall (labelled as multi-poles in figure 5c) escapes from the surface every 5-10 cycles, generating a high-stress peak in the sub-surface region.
(ii)- given previous argument (i), the separation event concerns a crystalline zone the size of the multi-pole thickness parallel to the Burgers vector (20-100 nm). Thus, the associated damaged zones are most probably small enough to remain stable once the crystal planes are separated locally. This process cannot lead to catastrophic cleavage of the whole PSB plane.

With the proposed crack initiation scheme, a transition exists between a prior extrusion-intrusion growth stage and a micro-crack initiation stage. The prior stage corresponds to the time needed to produce both thick enough multi-poles and sharp enough surface markings, the latter producing a gradual increase of stress tri-axiality. Here, there is however no clear transition between early crack initiation and subsequent mode-2 propagation in the surface grains: they both result from the same mechanism. Then, crack propagation proceeds in surface grain when the (large enough) dipolar walls come in succession at the tip of the crack. The crack propagation rate associated with such a mechanism is comprised within a range of 2 to 20 nm per cycle, corresponding to one 20-100 nm thick wall leaving the crystal every 5-10 cycles. These values are quite consistent with the short crack propagation rates observed

for this material, i.e. between 1 to 10 nm per cycle, for $\Delta\varepsilon_p = 10^{-3}$ [44]. The proposed scheme is also consistent with the TEM observations by Katagiri *et al*. [45], providing direct evidence of the relationship between the persistent slip band dislocation structure and fatigue crack in the earliest stage.

Finallyn experimental results from Ma and Laird [6] and Obrtlik *et al.* [44] show that the crack propagation rate has a weak link to $\Delta\varepsilon_p$, within the range $10^{-5}<\Delta\varepsilon_p<10^{-3}$. In the future, the present model could address these (and other) effects for further validations and to provide insight into the underlying physical process.

4 SUMMARY

DDD fatigue simulations under symmetrical loading have been performed, for various loading ranges up to $\Delta\varepsilon_p = 10^{-3}$ and grain sizes up to 22 μm. The surface slip markings associated with the dislocation microstructures have been computed using a post-processing method taking advantage of the edge-screw discretization in the DDD framework used here.

This way, it is found that the persistent surface slip markings are positioned at the intersection between the persistent slip bands inside the grain and the surface, where dislocation original channel arrangements are present. The persistent markings obtained are tongue like, with a tongue size of the same diameter as the channel cross-section. After strain localisation in the form of PSB, reversible slip activity persists at the PSB-matrix edges, where interface pile-ups are present.

By comparison with experimental data, slip is found to be an important contribution to the early extrusion growth rate ($N < 2000$). Persistent surface marking growth rate is a linear function of the strain range and grain size. The individual slip marking characteristics are exactly the same in either double or single slip, due to higher cross slip probability associated with the latter case. The presence of a mean stress results in a larger extrusion growth rate as observed in symmetrical loading conditions, for the same plastic strain range.

Micro-crack initiation conditions are analyzed using DDD results. In spite of the differences between earlier coarse-slip models and the present model, a similar extrusion (intrusion) random walk growth regime is obtained. Analysis of the stress (or energy) concentrations is

performed, assuming that the local crystal distortion stress (or energy) concentrations in the crystal contribute to micro-crack initiation. The analysis results reveal that the most favourable conditions for micro-crack initiation arise when a multi-polar wall from the PSB channels approaches the surface markings. This led to the proposition of a new micro-crack initiation scheme, combining the different model types existing in the literature.

APPENDIX-1 EFFECT OF FREE SURFACE BOUNDARY CONDITIONS

In this section, some of the results as presented in section 3 are compared with simulations using completely different surface boundary conditions, i.e. using a flat and oxide-less crystal surface. In that case, the surface is traction-free and generates the so-called image-forces, in the crystal sub-surface region. These forces can be computed accurately using the superimposition principle, by coupling the DDD code with a finite element method computation code. The validity of this numerical approach has been established in the past, by comparison with rigorous analytical methods [29]. Even though other computation methods are available to treat such boundary condition problem, the proposed approach is yet the only one that is applicable to the fatigue simulations as performed in this work.

The superimposition principle applied to an oxide-free crystal surface consists to take the stress field in the crystal medium $\boldsymbol{\sigma}(M)$ as the sum of two stresses $\hat{\sigma}$ and $\tilde{\sigma}$ (see figureA1). The first component $\hat{\sigma}$ is created by the dislocations as if present in an infinite medium. The term $\hat{\sigma}$ is thus computed using the standard analytical expressions, generating non-vanishing forces inside the whole medium, including $\mathbf{F}^D$ forces in the top surface. The second component $\tilde{\sigma}$ is the solution of the elastic problem where the external loading ($-\mathbf{F}^D$) is applied on a perfectly elastic medium Ω. The stress field $\tilde{\sigma}$ is computed by means of finite element method. The resulting heterogeneous stress $\sigma(M) = \hat{\sigma}(M) + \tilde{\sigma}(M)$ is then applied to the dislocations segments present in medium Ω, in the dislocation code.

[Insert figureA1 about here]

When image forces are accounted for, the position (and time) of some individual cross-slip events are modified, up to 2 µm from the free surface. Consequently, the location and time at which the individual PSB are formed can be slightly changed. Otherwise, whenever stable PSB are created, they are made of exactly same channels, tangles and interfacial pile-ups structures as described in section 3.1.1, no matter the surface conditions. Quantitatively, the characteristic PSB thickness and mean spacing were found to be exactly the same, with or without image forces. In addition, comparison between figure A2a and A2b show little change in the individual persistent slip marking slip offset; growth rate and thickness. Although some of the surface steps visible in figure A2a (at the left side of the image) are not present figure A2b, none of these can be associated with stable PSB structures like interfacial pile-ups or channel multi-poles. Consequently, the additional steps observable in figure A2a are reversible and transient.

[Insert figureA2 about here]

In principle, the image-forces could significantly change the slip marking morphologies by triggering additional cross slip events, in the sub-surface region. In the simulations performed here however, the normal to the free surface is nearly collinear to the Burgers vector of the primary slip system (see figure 5). Therefore, the image forces acting on the screw segments are minimised. This may explains why the effect of a free surface on the slip marking morphologies is relatively small.

ACKNOWLEDGEMENTS

The present work originates from the Contrat Programme Recherche en Simulation des Matériaux pour les Installations et Réacteurs Nucléaires, a CNRS-CEA-Electricité de France joint program, whose financial support is gratefully acknowledged. The participation of the Réseau Matériaux and the Direction Recherche Technologique (CEA/DRT) through the research project FAMICRO, is also acknowledged.

FIGURE CAPTIONS

Figure 1. Calculation of the dislocation displacement field. (a) Barnett's expression for the displacement field coming from a triangular loop, (b) application of Barnett's expression to an arbitrary shaped loop, made of discrete screw and edge segments.

Figure 2. Surface step formation due to dislocation elimination at the surface. (a) Actual case, (b) Numerical modelling.

Figure 3. Influence of the virtual dislocation standoff distance on the calculated surface profile. (a) Calculation framework, (b) calculated profiles for different standoff distances.

Figure 4. Surface slip marking evolution during the cycles computed at the same position. Note the gradual formation of the extrusion. Results obtained in symmetrical, single slip loading conditions, $\Delta\varepsilon_p = 10^{-3}$, grain diameter = 5 µm (cylindrical geometry).

Figure 5. Different views of a typical persistent slip band dislocation microstructure with associated surface displacements. (a) Viewed in perspective, (b) viewed from a direction perpendicular to the primary slip system, (c) viewed from a direction perpendicular to surface slip marking. Results obtained in symmetrical, single slip loading conditions, $\Delta\varepsilon_p = 10^{-3}$, grain diameter = 5 µm (cylindrical geometry). Cycle N = 23.

Figure 6. Details of the tongue-like surface slip markings associated with the PSB structures. (a) Viewed in perspective, (b) viewed from a direction perpendicular to the grain surface.

Results obtained in symmetrical, single slip loading conditions, $\Delta\varepsilon_p = 10^{-3}$, grain diameter = 5 µm (cylindrical geometry), Cycle N = 23.

Figure 7. Sketch of the simplified automatic calculation method used to compute the surface displacements. The sign of quantity *a* depends on the virtual dislocation line vector.

Figure 8. Surface displacement evolutions. (a) Double- versus single-slip conditions. The quantity M^p/M^s is the ratio between the resolved shear stress in primary and deviate slip systems. In single slip $M^p/M^s = 3$, in double slip $M^p/M^s = 1$. (b) Effect of mean strain ε^{moy}, in non-symmetrical fatigue, in single-slip loading conditions. Results obtained for a grain diameter = 5 µm (cylindrical geometry).

Figure 9. Computation results associated with a test volume a = 0,5 µm, positioned inside the PSB channel, near the channel-surface intersection. (a) Two typical energy density distribution histograms computed at cycle 5 and cycle 19, (b) mean energy density evolution, (c) maximum energy density evolution. Results obtained in single-slip loading conditions, with $\Delta\varepsilon_p = 10^{-3}$, grain diameter = 5 µm (cylindrical geometry).

Figure 10. Standard deviation stress magnitude evolutions during the cycles, inside the same test volume as in figure 9. (a) Resolved shear stress component, (b) stress component normal to the primary slip plane. Results obtained in single slip loading conditions, with $\Delta\varepsilon_p = 10^{-3}$, grain diameter = 5 µm (cylindrical geometry).

Figure 11. Evolution of the characteristic dimensions of the individual persistent slip markings, for two simulated grain shapes. (a) The surface relief accumulation depends

linearly on the grain depth. (b) Evolution of the extrusion width *e*. Results obtained in single slip loading conditions, with a grain diameter = 5 µm (cylindrical geometry), $\Delta\varepsilon_p = 10^{-3}$.

Figure A1. Superimposition principle and image force calculation for an oxide-free crystal surface. For computation of the stress field $\tilde{\sigma}$ on medium Ω, specific conditions are applied to the nodes in the bottom surface in order to avoid the rigid body trivial solution.

Figure A2. Details of the permanent surface slip markings associated with the PSB structures. (a) Surface displacements without image-forces and (b) with image forces. These results are obtained in single-slip loading conditions, with $\Delta\varepsilon_p = 10^{-3}$, grain diameter = 5 µm (cylindrical geometry), at exactly the same location in the simulated crystal surface and the same cumulated plastic strain.

FIGURE-1

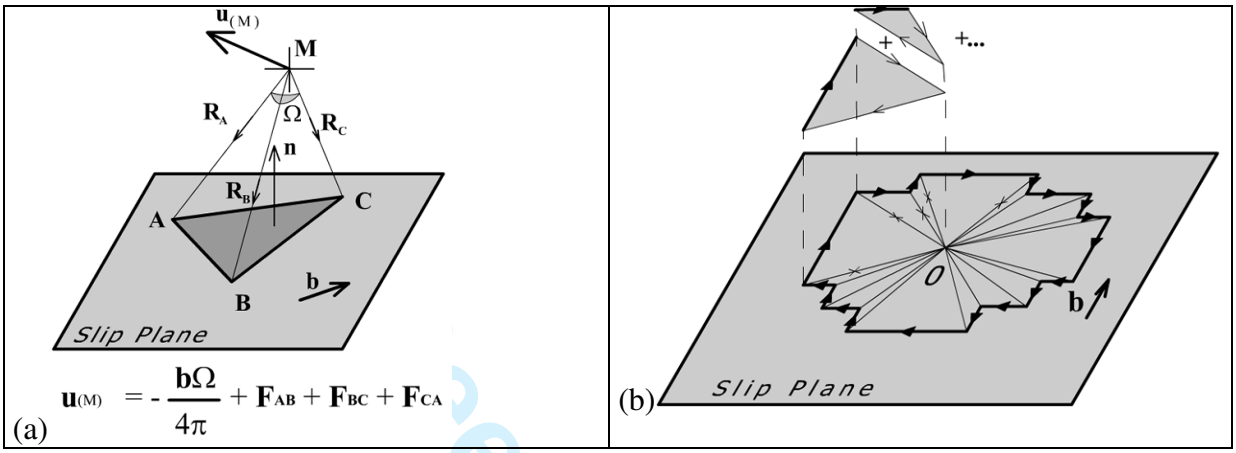

FIGURE-2

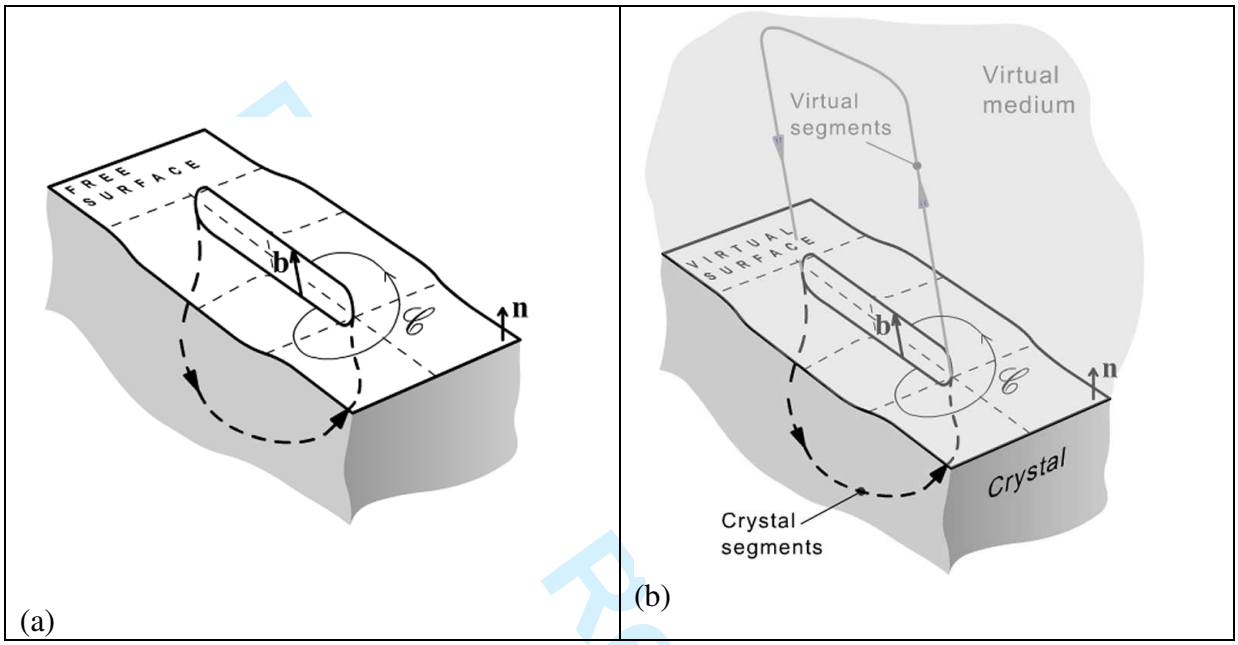

FIGURE-3

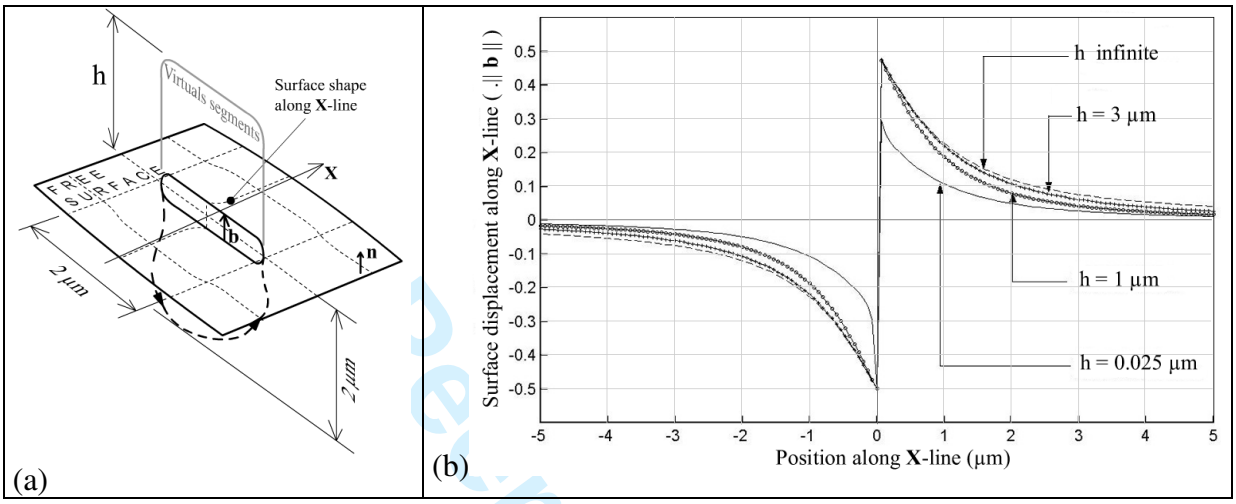

FIGURE-4

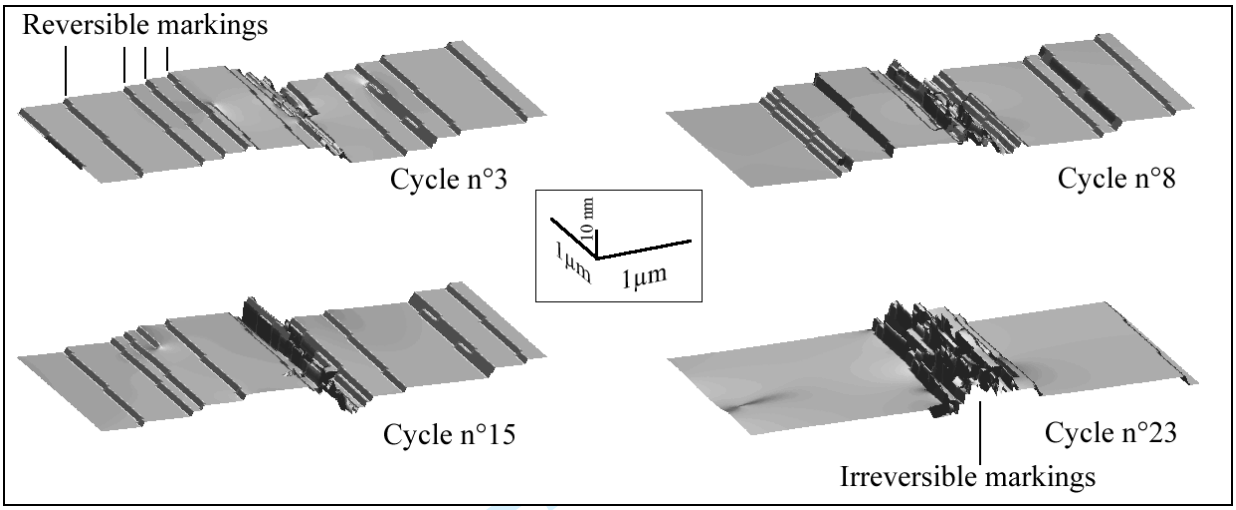

FIGURE-5

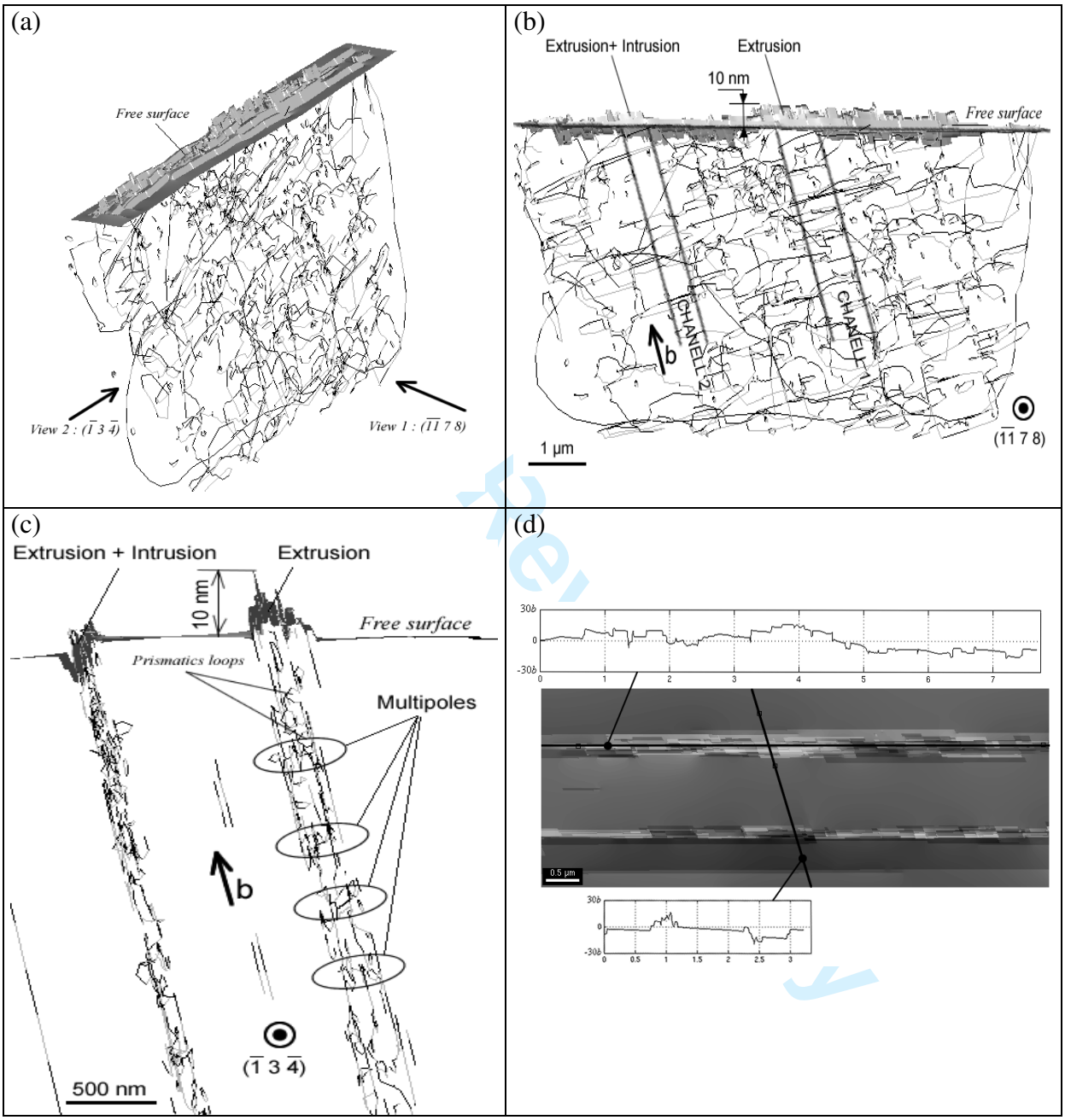
(a)
Free surface
View 2 : (1̄ 3 4̄)
View 1 : (11̄ 7 8)
(b)
Extrusion+ Intrusion
Extrusion
10 nm
Free surface
CHANEL 2
CHANEL 1
b
(11̄ 7 8)
1 µm
(c)
Extrusion + Intrusion
Extrusion
10 nm
Free surface
Prismatics loops
Multipoles
b
(1̄ 3 4̄)
500 nm
(d)
30b
0
-30b
0.5 µm

FIGURE-6

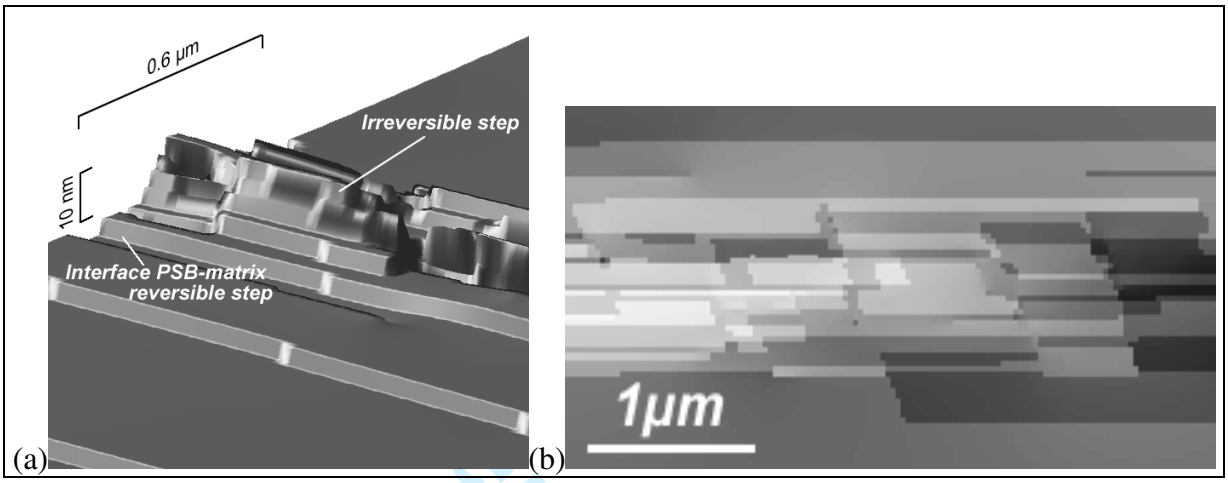

FIGURE-7

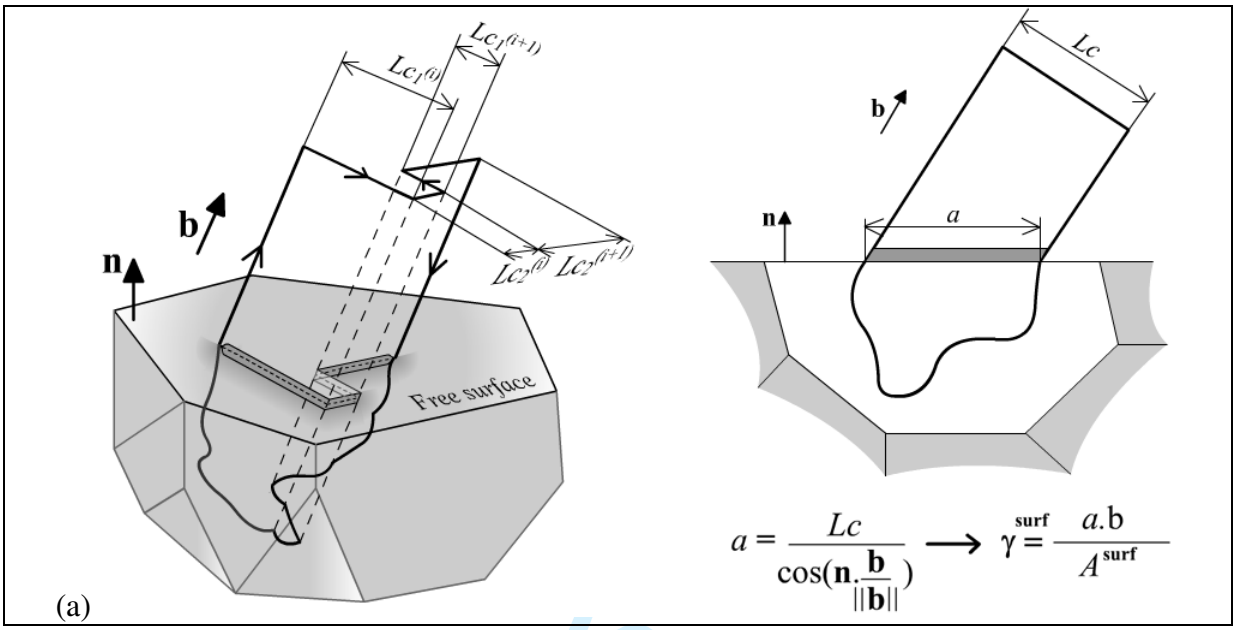

FIGURE-8

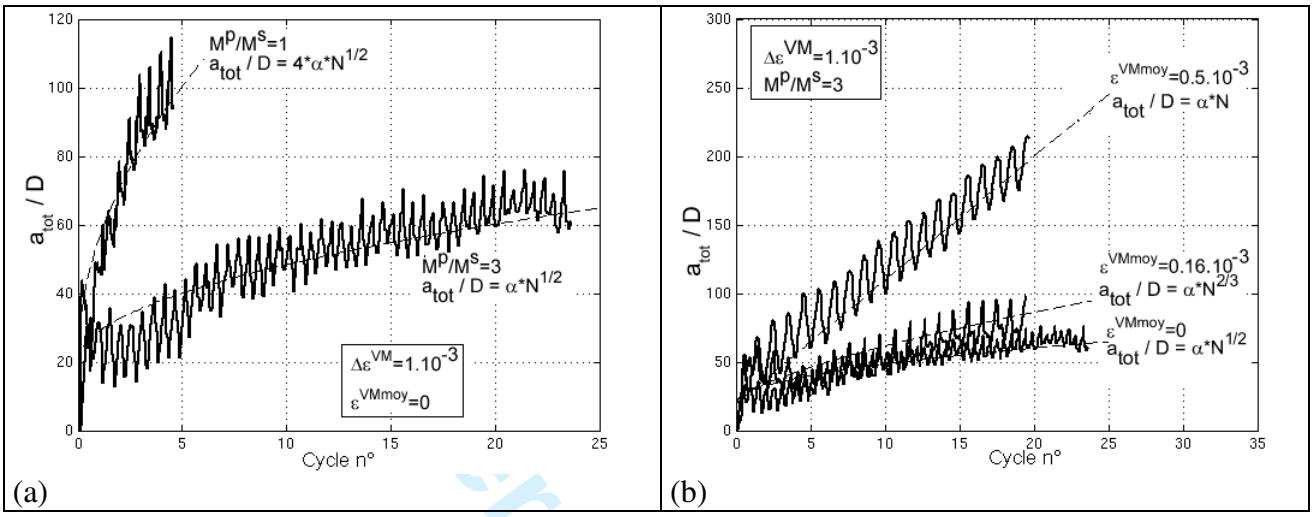

FIGURE-9

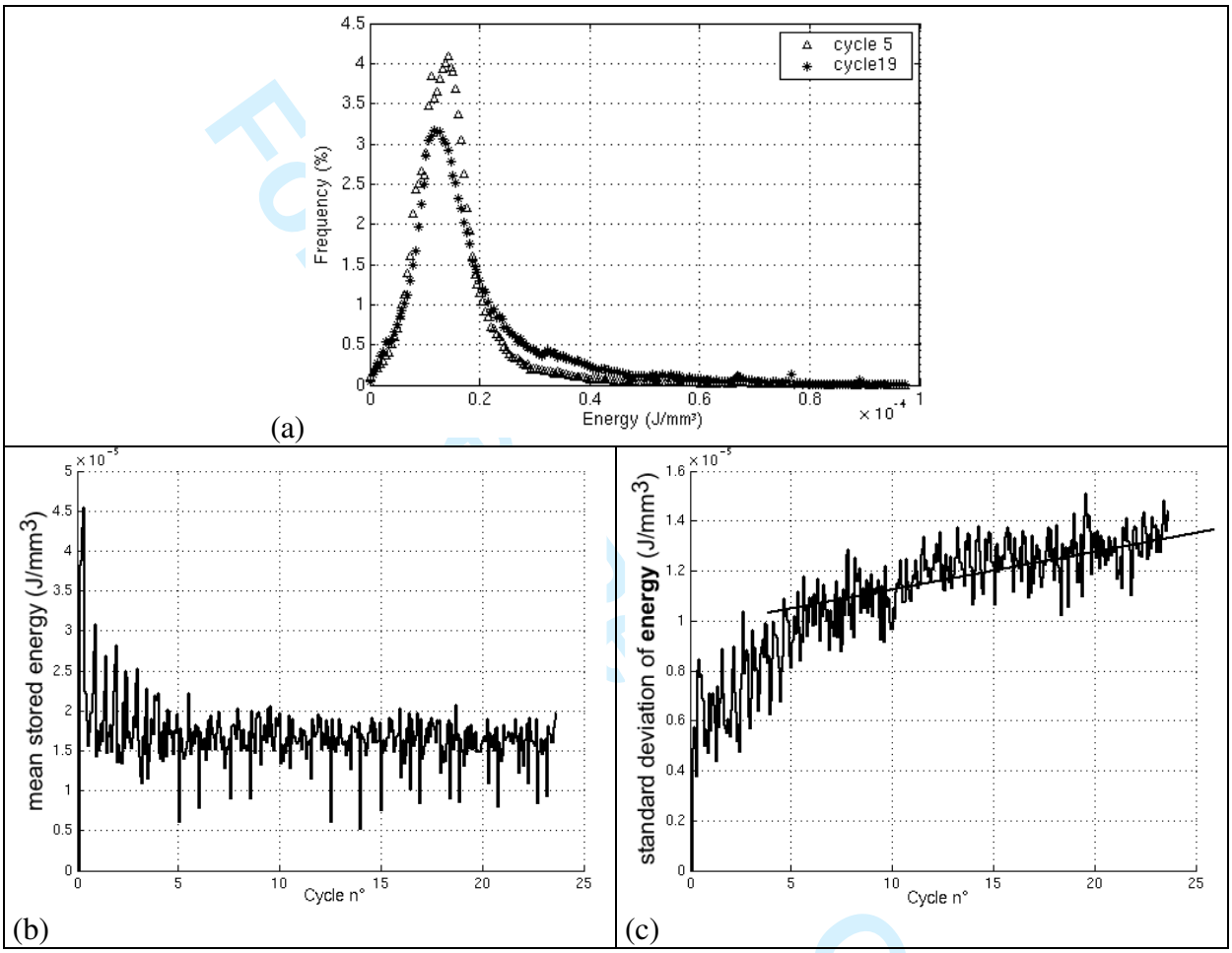
cycle 5
cycle19
Frequency (%)
Energy (J/mm³)
× 10⁻⁴
(a)
mean stored energy (J/mm³)
× 10⁻⁵
Cycle n°
(b)
standard deviation of energy (J/mm³)
× 10⁻⁵
Cycle n°
(c)

FIGURE-10

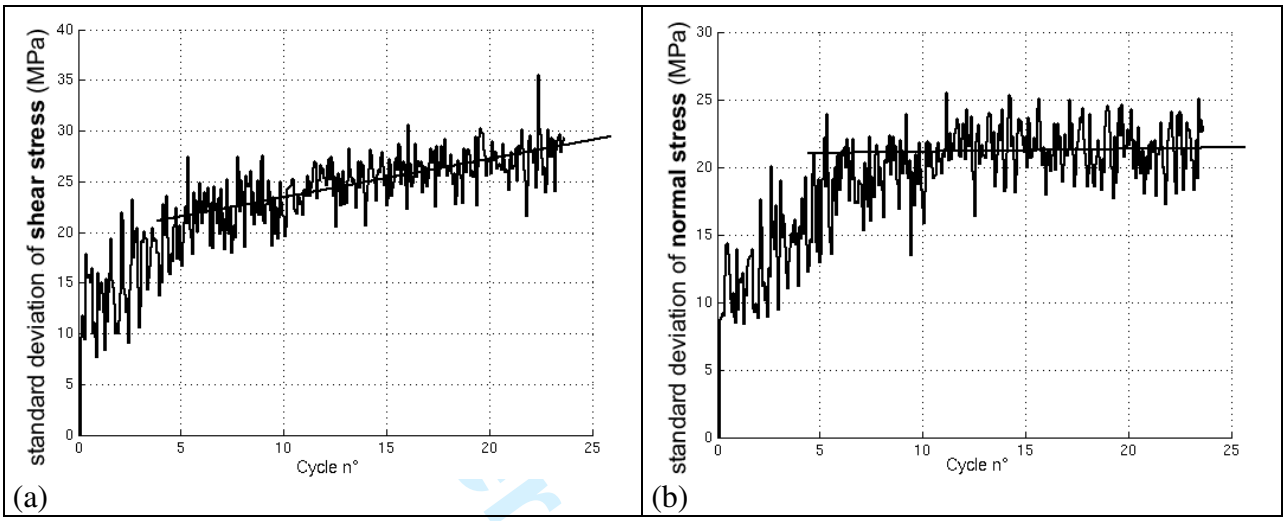

FIGURE-11

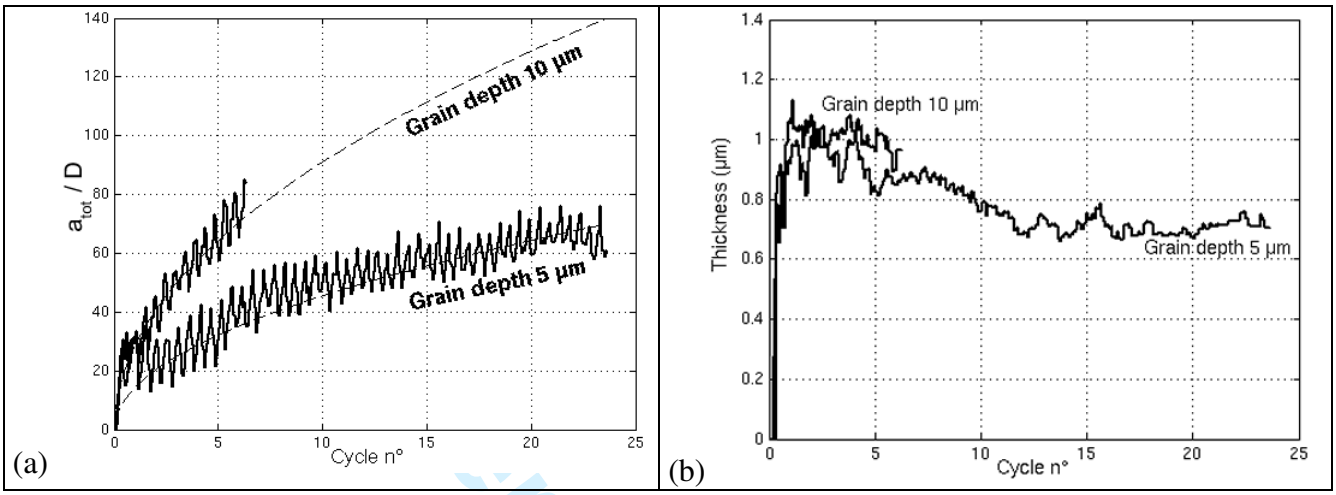

FIGURE-A1

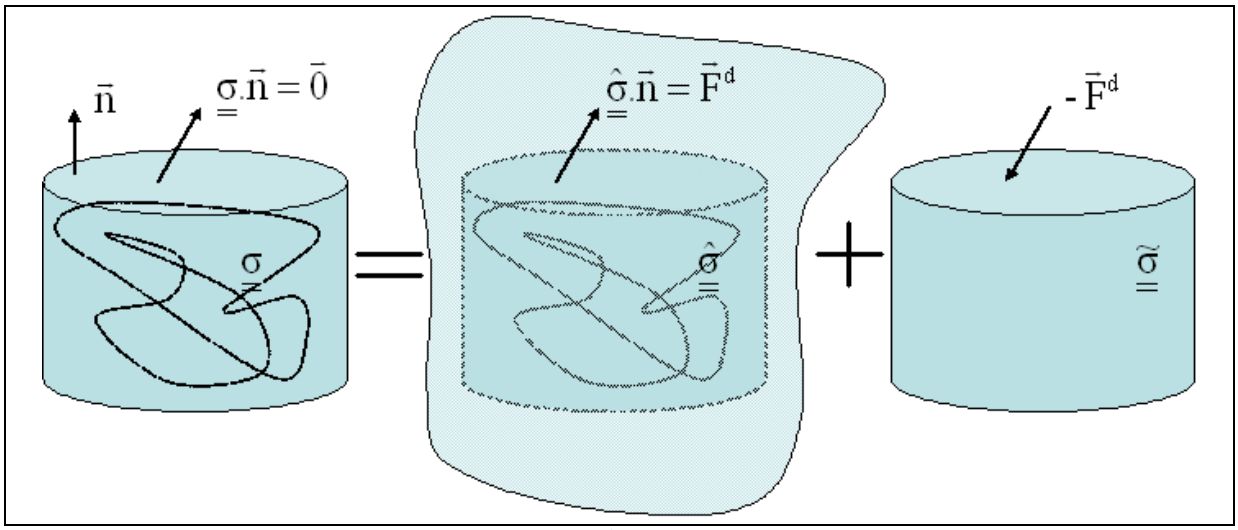

FIGURE-A2

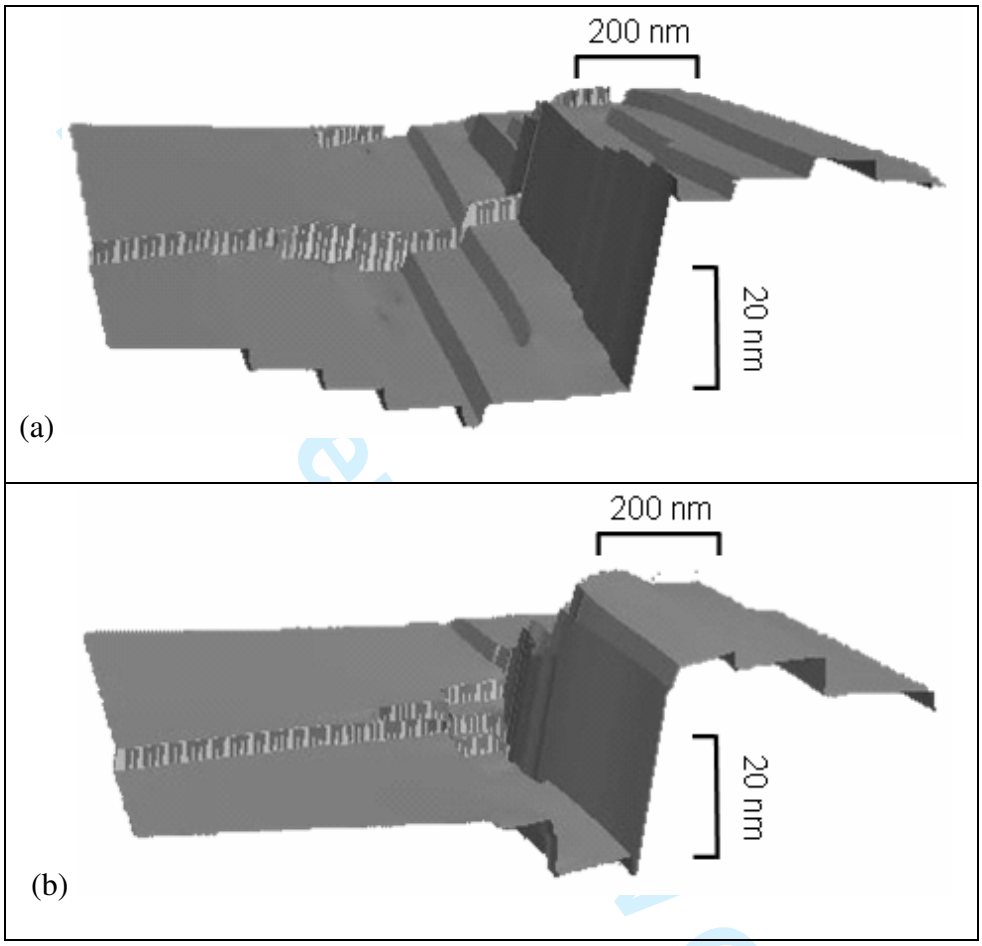

REFERENCES.

[1] J. Man, K. Obrtlik, C. Blochwitz and J. Polak, Acta mater. **50** 3767 (2002).

[2] H. Mughrabi, *Dislocation Properties in Real Materials, Book No. 323* (The Institute of Metals, London, p. 244, 1985).

[3] C. Laird, Fatigue, *Physical Metallurgy*, Fourth edition, (Elsevier Science, edited by R.W. Cahn, & P. Haasen, p. 2294 1996).

[4] S. Suresh, *Fatigue of Materials*, Second edition, (Cambridge University Press, Cambridge 1998).

[5] Z.S. Bazinski and S.J. Basinski, Acta Metall. Mater. **33** 1319 (1985).

[6] B-T. Ma and C. Laird, Acta Metal. Mater. **37** 325 (1989).

[7] L. Cretegny and A. Saxena Acta Mater. **49** 3755 (2001).

[8] J. Man, K. Obrtlik and J. Polak, Mat. Sci. Eng. A **351** 123 (2003).

[9] K. Obrtlik, T. Kruml and J. Polak, Mat. Sci. Eng. A **187** 1 (1994).

[10] M. Gerland and P. Violan, Mat. Sci. Eng. A **84** 23 (1986).

[11] M. Gerland, R. Alain, B. Ait Saadi and J. Mendez, Mat. Sci. Eng. A **229** 68 (1997).

[12] Y. Li and C. Laird, Mat. Sci. Eng. A **186** 87 (1994).

[13] Y. Li and C. Laird, Mat. Sci. Eng. A **186** 65 (1994).

[14] L. Kubin and G. Canova, Scripta Metall. **27** 957 (1992).

[15] J.P. Hirth, M. Rhee and H.M. Zbib, J. Comput. Aided Mater. Des. **3** 164 (1996).

[16] K.W. Schwarz , Phys. Rev. Lett. **78** 4785 (1997).

[17] B. Devincre and L.P. Kubin, Mat. Sci. Eng. A **234-236** 8 (1997).

[18] M. Verdier, M. Fivel and I. Groma, Modelling Simul. Mater. Sci. Eng. **6**(6) 755 (1998).

[19] L.Z. Sun, N.M. Ghoniem, S-H. Tong and B.N. Singh, J. Nucl. Mat., **283-287**, 741 (2000).

[20] H.M. Zbib, M. Rhee, J.P. Hirth and T.D. de la Rubia, J. Mech. Behavior of Mat. **11** 251 (2000).

[21] C. Robertson, M.C. Fivel and A. Fissolo, Mat. Sci. Eng. A **315** 47 (2001).

[22] M.C. Fivel, C.F. Robertson, G.R. Canova and L. Boulanger, Acta mater. **46** 6183 (1998).

[23] S. Groh, B. Devincre, L.P. Kubin, A. Roos, F. Feyel and J-L. Chaboche, Phil. Mag. Letters **83** 303 (2003).

[24] P. Pant, K.W. Schwarz and S.P. Baker, Acta Mater. **51** 3243 (2003).

[25] D. Weygand, L.H. Friedman, E. Van der Giessen and A. Needleman, *Modelling Simul. Mater. Sci. Eng.* **10** 437 (2002).

[26] C. Déprés, M.C. Fivel, C. Robertson, A. Fissolo and M. Verdier, J. Phys IV France **106** 81 (2003).

[27] C. Déprés, C.F. Robertson M.C. Fivel, Phil. Mag. A **84** 2257 (2004).

[28] V. Lubarda V., J.A. Blume and A. Needleman, Acta metall. mater. **41** 625 (1993).

[29] M.C. Fivel, T.J. Gosling and G.R. Canova, Modelling Simulation Mater. Sci. Eng.. **4** 581 (1996).

[30] I. Kwon, M. Fine and J. Weertman, Acta Metall. Mater. **37** 2937 (1989).

[31] R. Wang, H. Mughrabi, S. Mc Govern and M. Rapp, Mater. Sci. Eng. **65** 219 (1984).

[32] H. Hunsche and P. Neumann, *Basic Questions in Fatigue*: vol. 1, ASTM STP 924, (Philadelphia (PA), edited by JT. Fong & RJ. Fields, p. 26 1988).

[33] D.E. Witmer, G.C. Farrington, C. Laird, Acta Metall. Mater. **42** 3493 (1987).

[34] D.M. Barnett, Phil. Mag. A **51** 3 (1985).

[35] S. Brochard, P. Beauchamp and J. Grilhé, Phys. Rev. B **61** 13(2000).

[36] P. Lukas, *ASM Handbook: Fatigue and Fracture*, Vol. 19, (edited by ASM International, pp. 96-109, 1996).

[37] W.A. Wood, *Fatigue of Aircraft Structures*, (Academic Press, New York 1956).

[38] May A.N., Nature **185** 303 (1960).

[39] P. Neumann, Acta Metall. Mater. **17** 1219 (1969).

[40] K. Differt, U. Essmann and H. Mughrabi, Phil. Mag. A **54** 237 (1986).

[41] S.N. Rosenbloom and C. Laird, Acta Metall. Mater. **41**(12) 3473 (1993).

[42] T. Mura, Mat. Sci. Eng. A **176** 61 (1994).

[43] M. Mineur, P. Villechaise and J. Mendez, Mat. Sci. Eng. A **286** 257 (2000).

[44] K. Obrtlik, J. Polak, M. Hajek and A. Vasek, Int. J. Fatigue **6** 471 (1997).

[45] K. Katagiri, A. Omura, K. Koyanagi, J. Awatani, T. Shiraishi and H. Kaneshiro, Metall. Trans. **8A** 1769 (1976).